

Computational framework for direct numerical simulation of shock-turbulence interaction in thermochemical nonequilibrium

By C. T. Williams, M. Di Renzo[†] AND P. Moin

1. Motivation and objectives

Dissipation of kinetic energy in hypersonic flows activates a number of thermochemical processes, including both chemical dissociation and vibrational excitation. As chemical reactions and thermal relaxation proceed at finite rates, on timescales comparable to those of the hydrodynamic field, hypersonic flows are largely characterized as in a state of thermochemical nonequilibrium (Candler 2019; Di Renzo & Urzay 2021; Passiatore *et al.* 2022). In hypersonic flows, thermal nonequilibrium is most significant in the vicinity of shock waves, across which preferential excitation of rotational and translational internal energy modes initiates vibrational relaxation in the post-shock region. As the internal excitation of molecular species and reaction rates of dissociation are fundamentally coupled (Park 1990), the chemical composition of the post-shock gas strongly depends on the vibrational relaxation process. The post-shock evolution of the thermochemical variables couples to the hydrodynamic field via the equation of state, inducing a mean post-shock pressure gradient. Excitation of vibrational-electronic energy modes has been shown to strongly impact the spectra of post-shock pressure fluctuations in shock/boundary-layer interactions (Di Renzo *et al.* 2022), though the effect of finite-rate vibrational relaxation on pressure fluctuations remains uncharacterized. Indeed, numerical investigations of vibrational relaxation in shock-dominated flows consist almost entirely of either laminar or inviscid analyses, and, as such, the impact of thermochemical relaxation on shock-turbulence interactions requires further investigation.

In the absence of high-enthalpy effects, direct numerical simulation has long been applied to investigate shock-turbulence interaction, elucidating the impact of turbulent fluctuations on shock structure, delineating the corresponding effect of the interaction on the post-shock turbulence and identifying the limitations of linear analysis. Lee *et al.* (1993) performed the first numerical simulation of shock-turbulence interaction, confirming the amplification of transverse vorticity components, as well as turbulent kinetic energy, across the shock. Subsequently, Mahesh *et al.* (1997) and Lee *et al.* (1997) characterized the impact of Mach number and upstream entropy fluctuations on shock-turbulence interactions, respectively. More recently, Larsson & Lele (2009) revisited shock-turbulence interaction with direct numerical simulation, correcting prior characterizations of post-shock anisotropy in vorticity variances and Reynolds stresses, in addition to identifying parameter ranges for which incoming turbulence can locally disrupt the normal shock. While the preceding studies considered only shock-turbulence interactions in calorically perfect gases, Huete *et al.* (2021) performed linear interaction analysis of high-enthalpy shock-turbulence interactions under the assumption of thermochemical equilibrium. As

[†] University of Salento, Italy

such, further characterization of canonical shock-turbulence interaction with finite-rate chemistry, vibrational relaxation and nonlinear interactions remains necessary.

In order to enable direct numerical simulation of shock-turbulence interactions in thermochemical nonequilibrium, the present study introduces a novel computational framework comprised of a low-dissipation hybrid scheme for evaluation of inviscid fluxes and two-temperature characteristic boundary conditions for inhomogeneous flows. Thermochemical nonequilibrium is modeled using the two-temperature approach of Park (1990), diffusion fluxes are computed with a second-order central scheme, and time advancement is performed using a third-order, strong-stability-preserving Runge-Kutta method. This computational framework has been implemented in the Hypersonics Task-Based Research (HTR) solver (Di Renzo *et al.* 2020; Williams *et al.* 2021).

The remainder of this brief is structured as follows. Section 2 introduces the relevant set of conservation equations, while Section 3 describes the hybrid scheme utilized for computation of Euler fluxes for nonequilibrium hypersonic flows. Section 4 presents the characteristic boundary conditions utilized for outflow boundaries, and Section 5 applies the computational framework to direct numerical simulation of shock-turbulence interaction in thermochemical nonequilibrium. Finally, Section 6 presents conclusions and articulates directions for future research.

2. Conservation equations

One of the classic approaches for modeling the effect of finite-rate relaxation of internal energy modes in hypersonic flows is the multitemperature formulation of the conservation equations, for which each energy mode is characterized by a Boltzmann distribution with a distinct temperature (Park 1990). In the present study, we utilize the two-temperature approach, for which the rotational and translational energies are both characterized by a common temperature T , while the vibrational and electronic energies are likewise assumed to be in equilibrium at a distinct temperature T_{ve} (Gnoffo *et al.* 1989; Park 1990). The corresponding conservation equations for hypersonic flows in thermochemical nonequilibrium can then be expressed as

$$\frac{\partial(\rho Y_i)}{\partial t} + \nabla \cdot (\rho Y_i \mathbf{u}) = -\nabla \cdot (\rho Y_i \mathbf{V}_i) + \dot{w}_i \quad i = 1, \dots, N_s, \quad (2.1)$$

$$\frac{\partial(\rho \mathbf{u})}{\partial t} + \nabla \cdot (\rho \mathbf{u} \mathbf{u}) = -\nabla P + \nabla \cdot \bar{\boldsymbol{\tau}}, \quad (2.2)$$

$$\frac{\partial(\rho e_0)}{\partial t} + \nabla \cdot (\rho e_0 \mathbf{u}) = \nabla \cdot \left(-\mathbf{u} P + \bar{\boldsymbol{\tau}} \mathbf{u} + \lambda_{tr} \nabla T + \lambda_{ve} \nabla T_{ve} - \rho \sum_{i=1}^{N_s} Y_i \mathbf{V}_i h_i \right), \quad (2.3)$$

$$\frac{\partial(\rho e_{ve})}{\partial t} + \nabla \cdot (\rho e_{ve} \mathbf{u}) = \nabla \cdot \left(\lambda_{ve} \nabla T_{ve} - \sum_{i=1}^{N_s} \rho Y_i \mathbf{V}_i e_{ve,i} \right) + \rho \sum_{i=1}^{N_s} Y_i \frac{e_{v,i}^* - e_{v,i}}{\tau_i} + \dot{w}_{ve}, \quad (2.4)$$

where the notation from Williams *et al.* (2021) has been maintained for consistency in the present report. The thermochemical modeling approach, computation of molecular transport properties and evaluation of chemical reaction rates also remain consistent with the treatment presented in Williams *et al.* (2021), with the nonpreferential vibration-dissociation coupling of Candler & MacCormack (1991) utilized for the present study. In order to verify the implementation of the thermochemical modeling approach, numerical simulations of triply periodic baths of air and nitrogen (Maier *et al.* 2021) sub-

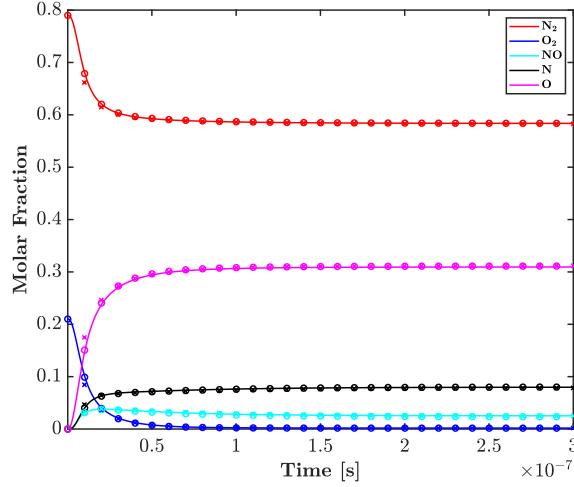


FIGURE 1. Evolution of chemical composition versus time for triply periodic bath of air. Present results (solid lines) are compared against the previous results of Gimelshein *et al.* (2022), with the LeMANS solver, (“x”-markers) and Maier *et al.* (2021) (“o”-markers).

ject to thermochemical relaxation are performed. For these test cases, Williams *et al.* (2021) previously demonstrated close agreement between the HTR solver and the reference solutions in terms of the temporal evolution of the translational-rotational and vibrational-electronic temperatures. Figures 1 and 2 confirm the performance of the HTR solver’s two-temperature thermochemical modeling, comparing the predicted time history of chemical composition against the respective results of Maier *et al.* (2021) and Gimelshein *et al.* (2022) for nonpreferential vibration-dissociation coupling. Particularly close agreement is observed among the reference results and the present study for the dissociating bath of air. Close alignment between the numerical solution from HTR and that of Maier *et al.* (2021) is likewise observed in the case of the nitrogen bath undergoing coupled dissociation/vibrational-relaxation as well.

3. Hybrid skew-symmetric scheme

In the present computational framework, Euler fluxes are evaluated with a hybrid method consisting of a sixth-order skew-symmetric scheme (Pirozzoli 2010) combined with sixth-order targeted essentially nonoscillatory (TENO) (Fu *et al.* 2016) shock capturing. Elementary fluxes for the TENO reconstruction are computed with the local Lax Friedrichs scheme, with further details on the flux reconstruction procedure for hypersonic two-temperature flows provided in Williams *et al.* (2021). In this hybrid scheme, the skew-symmetric formulation is deployed in the smooth regions of the flow, while the TENO reconstruction is utilized for stencils that cross shock waves. Activation of the TENO scheme is controlled by a directional shock sensor, which is defined for the generic variable ϕ as follows. First, the sub-stencil smoothness measures (γ_i) of the TENO6-A scheme are computed as

$$\gamma_i = \left(1 + \frac{\tau_6}{\beta_i + \epsilon} \right)^6, \quad (3.1)$$

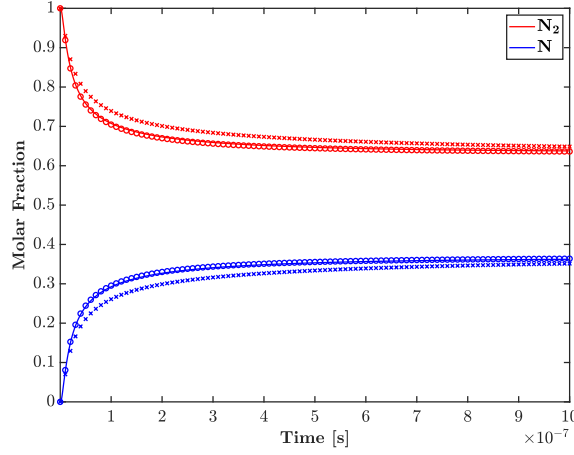


FIGURE 2. Evolution of chemical composition versus time for triply periodic bath of nitrogen. Present results (solid lines) are compared against the previous results of Gimelshein *et al.* (2022), with the LeMANS solver, (“x”-markers) and Maier *et al.* (2021) (“o”-markers).

where $\epsilon = 10^{-8}$ is a small number required to avoid division by zero. The smoothness indicators β_i for each of the four sub-stencils considered in this scheme are computed as

$$\begin{aligned}
 \beta_1 &= \left[\frac{13}{12} (\phi^{i-1} - 2\phi^i + \phi^{i+1}) + \frac{3}{12} (\phi^{i-1} - \phi^{i+1}) \right], \\
 \beta_2 &= \left[\frac{13}{12} (\phi^i - 2\phi^{i+1} + \phi^{i+2}) + \frac{3}{12} (3\phi^i - 4\phi^{i+1} + \phi^{i+2}) \right], \\
 \beta_3 &= \left[\frac{13}{12} (\phi^{i-2} - 2\phi^{i-1} + \phi^i) + \frac{3}{12} (3\phi^i - 4\phi^{i-1} + \phi^{i-2}) \right], \\
 \beta_4 &= \left[\frac{1}{36} (-11\phi^i + 18\phi^{i+1} - 9\phi^{i+2} + 2\phi^{i+3}) \right. \\
 &\quad \left. + \frac{13}{12} (2\phi^i - 5\phi^{i+1} + 4\phi^{i+2} - \phi^{i+3}) \right. \\
 &\quad \left. + \frac{781}{720} (-\phi^i + 3\phi^{i+1} - 3\phi^{i+2} + \phi^{i+3}) \right],
 \end{aligned} \tag{3.2}$$

where the superscript utilized for the variable ϕ indicates the index of the computational point along the direction for which the sensor is evaluated (Jiang & Shu 1996). In Eq. (3.1), τ_6 represents the smoothness indicator of the overall six-point stencil, which is computed as $\tau_6 = |\beta_4 - (\beta_3 + \beta_2 + 4\beta_1)/6|$ (Lusher & Sandham 2021). In analogy with the TENO reconstruction (Fu *et al.* 2016), the sensor will detect a shock if any one of the conditions

$$\frac{\gamma_i}{\sum_{j=1}^3 \gamma_j} < C_T, \quad \text{for } i = 1, 2, 3, \tag{3.3}$$

is satisfied. In Eq. (3.3), C_T is a cutoff parameter that is computed as a function of Φ , the maximum value across the six-point sensor stencil of the Ducros sensor. The cutoff parameter is evaluated as

$$C_T = 10^{-\lfloor 12.5 - 8.5(1-d) \rfloor}, \tag{3.4}$$

where $\lfloor \cdot \rfloor$ denotes the floor function, while $d = (1 - \Phi)^{10} (1 + 10\Phi)$ is a decay function designed to adapt the cutoff parameter based on the local flow physics. In particular, if

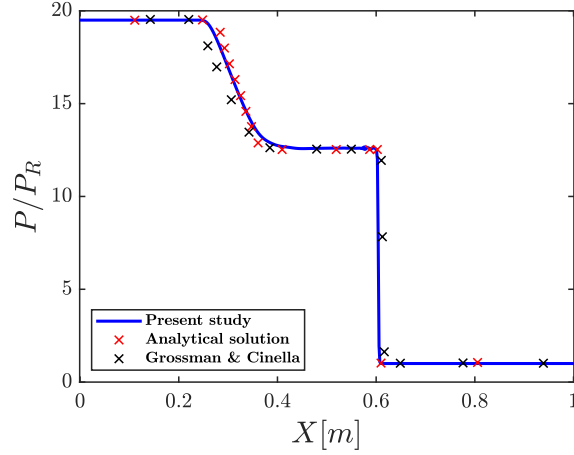


FIGURE 3. Pressure distribution in high-temperature shock tube from Grossman & Cinnella (1990).

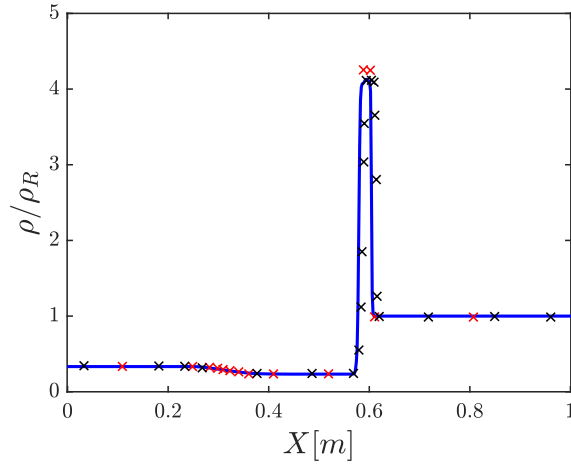


FIGURE 4. Density distribution in high-temperature shock tube from Grossman & Cinnella (1990).

the flow is locally dominated by rotation, Φ will tend to zero, d will tend to one and the cutoff parameter will approach 10^{-12} , reducing the likelihood of sensor activation. Conversely, if the fluid motion is locally dominated by compression, Φ will tend to one, d will tend to zero and the cutoff parameter will correspondingly approach 10^{-4} , which effectively eases fulfillment of the condition in Eq. (3.3). In the present formulation, the directional sensor is applied for each of the partial density fields and, if the sensor is triggered for a given direction in a grid point for any of the ρY_i fields, the numerical fluxes in that direction and corresponding to that grid point are discretized using the TENO flux reconstruction.

In order to verify the performance of the hybrid scheme, the reacting shock tube from Grossman & Cinnella (1990) has been simulated with the two-temperature HTR solver, with the results presented in Figures 3–6, depicting the distributions of pressure, density, velocity and vibrational energy, respectively. The reference analytical solution, which

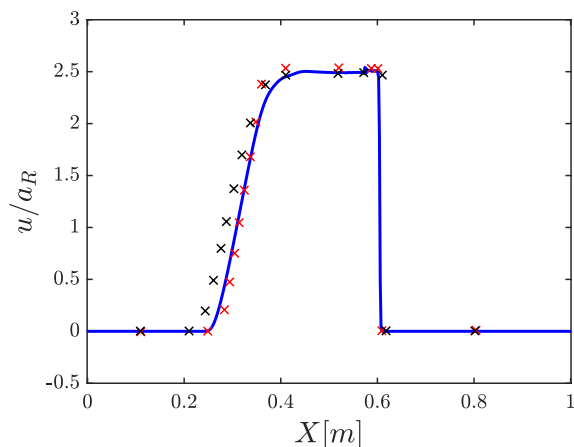


FIGURE 5. Velocity distribution in high-temperature shock tube from Grossman & Cinnella (1990).

assumed thermochemical equilibrium, is represented with red symbols, whereas the reference nonequilibrium numerical solution from Grossman & Cinnella (1990) is plotted in black symbols. Both sides of the initial Riemann problem are in thermochemical equilibrium, and so nonequilibrium effects are largely confined to the region immediately behind the traveling shock and to the expansion fan, where freezing of the vibrational-electronic modes is observed. The numerical solution from the HTR solver aligns closely with the analytical solution, confirming the performance of the hybrid scheme in this canonical two-temperature, multicomponent test case. Indeed, with the same number of grid points as the reference calculation, the present numerical scheme provides closer agreement with the analytical solution in terms of the velocity and pressure distributions, particularly in the vicinity of the expansion fan and shock front. Marginal differences are observed between the present results and the reference with respect to the vibrational energy distribution, but this can be reasonably attributed to the differences in vibrational-relaxation modeling approaches.

4. Characteristic boundary conditions

Extending the analysis of Okong'o & Bellan (2002), the present section introduces the set of characteristic boundary conditions for two-temperature hypersonic flows in thermochemical nonequilibrium. Developed from the relevant locally one-dimensional inviscid relations corresponding to the two-temperature conservation equations presented in Section 2, the characteristic boundary conditions enable consideration of inhomogeneous flows by mitigating the spurious reflection of waves at boundaries of the computational domain. At outflow boundaries, the relevant set of Navier-Stokes characteristic boundary conditions can be expressed for two-temperature, multicomponent flows as

$$\frac{\partial \rho u}{\partial t} + \rho d_2 + u d_1 = \frac{\partial \tau_{xx}}{\partial x} - \nabla_t \cdot (\rho v \mathbf{u}_t), \quad (4.1)$$

$$\frac{\partial \rho v}{\partial t} + \rho d_3 + v d_1 = -\frac{\partial P}{\partial y} + \nabla_t \cdot (\boldsymbol{\tau}_{yt}) - \nabla_t \cdot (\rho v \mathbf{u}_t), \quad (4.2)$$

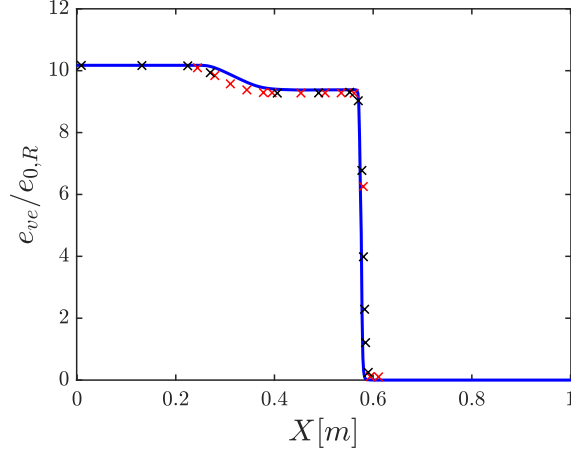


FIGURE 6. Vibrational energy distribution in high-temperature shock tube from Grossman & Cinnella (1990).

$$\frac{\partial \rho w}{\partial t} + \rho d_4 + w d_1 = -\frac{\partial P}{\partial z} + \nabla_t \cdot (\boldsymbol{\tau}_{zt}) - \nabla_t \cdot (\rho w \mathbf{u}_t), \quad (4.3)$$

$$\begin{aligned} \frac{\partial \rho e_0}{\partial t} + h_0 d_1 + \rho (u d_2 + v d_3 + w d_4) + \rho \bar{c}_{v,ve} d_5 + \rho \sum_{i=1}^{N_s} \left(h_i - \bar{c}_{p,tr} \frac{T \bar{M}}{\mathcal{M}_i} \right) d_{i+5} \\ + (\bar{c}_{p,tr} T) d_{N_s+6} = \frac{\partial (u \tau_{xx})}{\partial x} + \tau_{xy} \frac{\partial v}{\partial x} + \tau_{xz} \frac{\partial w}{\partial x} - \rho \sum_{i=1}^{N_s} Y_i V_{i,x} \frac{\partial h_i}{\partial x} \\ + \nabla_t \cdot \left(\bar{\boldsymbol{\tau}}_t \mathbf{u}_t + \lambda_{tr} \nabla_t T + \lambda_{ve} \nabla_t T_{ve} - \rho \sum_{i=1}^{N_s} Y_i \mathbf{V}_{i,t} h_i - \rho h_0 \mathbf{u}_t \right), \end{aligned} \quad (4.4)$$

$$\begin{aligned} \frac{\partial \rho e_{ve}}{\partial t} + e_{ve} d_1 + \rho \bar{c}_{v,ve} d_5 + \rho \sum_{i=1}^{N_s} e_{ve,i} d_{i+5} = \rho \sum_{i=1}^{N_s} Y_i \frac{e_{v,i}^* - e_{v,i}}{\tau_i} + \dot{w}_{ve} \\ - \rho \sum_{i=1}^{N_s} Y_i V_{i,x} \frac{\partial e_{ve,i}}{\partial x} + \nabla_t \cdot \left(\lambda_{ve} \nabla_t T_{ve} - \rho \sum_{i=1}^{N_s} Y_i \mathbf{V}_{i,t} e_{ve,i} - \rho e_{ve} \mathbf{u}_t \right), \end{aligned} \quad (4.5)$$

$$\frac{\partial \rho Y_i}{\partial t} + \rho d_{i+5} + Y_i d_1 = \dot{w}_i - \nabla_t \cdot (\rho Y_i (\mathbf{V}_{i,t} + \mathbf{u}_t)), \quad (4.6)$$

where $\nabla_t = [\partial/\partial y, \partial/\partial z]^T$ is defined as the transverse gradient operator, $\mathbf{u}_t = [v, w]^T$ is the transverse velocity vector, $\tau_{xx} = \hat{\mathbf{e}}_1^T \bar{\boldsymbol{\tau}} \hat{\mathbf{e}}_1$ is the viscous streamwise flux of streamwise momentum and $\mathbf{V}_{i,t} = [\hat{\mathbf{e}}_2, \hat{\mathbf{e}}_3]^T \mathbf{V}_i$ is the transverse diffusion velocity vector. Likewise, the transverse viscous stress tensor is then defined as

$$\bar{\boldsymbol{\tau}}_t = \begin{bmatrix} \tau_{yt} \\ \tau_{zt} \end{bmatrix} = [\hat{\mathbf{e}}_2, \hat{\mathbf{e}}_3]^T \bar{\boldsymbol{\tau}} [\hat{\mathbf{e}}_2, \hat{\mathbf{e}}_3]. \quad (4.7)$$

The variables d_1 through d_{N_s+6} are defined as follows

$$\begin{aligned}
d_1 &= \frac{1}{a^2} \left(\frac{\mathcal{L}_1 + \mathcal{L}_{N_s+6}}{2} - \mathcal{L}_2 \right), \\
d_2 &= \frac{1}{2\rho a} (\mathcal{L}_{N_s+6} - \mathcal{L}_1), \\
d_3 &= \mathcal{L}_3, \\
d_4 &= \mathcal{L}_4, \\
d_5 &= \mathcal{L}_5, \\
d_{i+5} &= \mathcal{L}_{i+5}, \quad i = 1, \dots, N_s, \\
d_{N_s+6} &= \mathcal{L}_2/a^2,
\end{aligned} \tag{4.8}$$

where $\mathcal{L}_1, \dots, \mathcal{L}_{N_s+6}$ are the wave-amplitude variations from the locally one-dimensional inviscid relations given by

$$\begin{aligned}
\mathcal{L}_1 &= (u - a) \left(\frac{\partial P}{\partial x} - \rho a \frac{\partial u}{\partial x} \right), \\
\mathcal{L}_2 &= u \left(\frac{\partial P}{\partial x} - a^2 \frac{\partial \rho}{\partial x} \right), \\
\mathcal{L}_3 &= u \frac{\partial v}{\partial x}, \\
\mathcal{L}_4 &= u \frac{\partial w}{\partial x}, \\
\mathcal{L}_5 &= u \frac{\partial T_{ve}}{\partial x}, \\
\mathcal{L}_{i+5} &= u \frac{\partial Y_i}{\partial x}, \quad i = 1, \dots, N_s, \\
\mathcal{L}_{N_s+6} &= (u + a) \left(\frac{\partial P}{\partial x} + \rho a \frac{\partial u}{\partial x} \right).
\end{aligned} \tag{4.9}$$

The frozen speed of sound of the mixture, a , is given by

$$a^2 = \left(\frac{\partial P}{\partial \rho} \right)_{s, Y_i, T_{ve}} = \left(\frac{\bar{c}_{p,tr}}{\bar{c}_{v,tr}} \right) \left(\frac{P}{\rho} \right), \tag{4.10}$$

where $\bar{c}_{p,tr}$ and $\bar{c}_{v,tr}$ are the mass-averaged specific heats at constant pressure and volume, respectively, corresponding to the rotational and translational energy modes. For the present study, the assumption of fully excited rigid rotation and translation implies

$$\bar{c}_{v,tr} = (3/2)R^0T/\bar{\mathcal{M}} + \sum_{i=1}^{N_s} Y_i \mathcal{V}_i R^0T/\mathcal{M}_i, \tag{4.11}$$

where $\bar{\mathcal{M}} = \left[\sum_{i=1}^{N_s} Y_i/\mathcal{M}_i \right]^{-1}$ is the average molecular weight of the mixture. The mass-averaged vibrational-electronic specific heat, $\bar{c}_{v,ve}$, is given by

$$\bar{c}_{v,ve} = \sum_{i=1}^{N_s} Y_i (c_{v,v,i} + c_{v,e,i}), \tag{4.12}$$

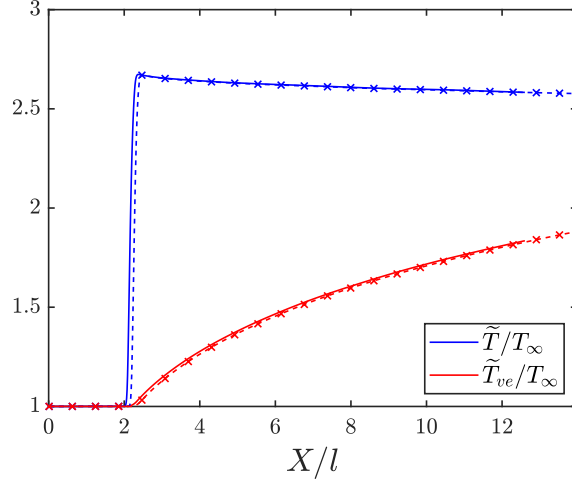


FIGURE 7. Favre-averaged temperature distributions for shock-turbulence interaction in thermochemical nonequilibrium.

where $c_{v,v,i}$ and $c_{v,e,i}$ are, respectively, the vibrational and electronic specific heats for species i . The electronic specific heat for each species can be evaluated with

$$c_{v,e,i} = \frac{R^0 T_{ve}}{\mathcal{M}_i} \left[2 \frac{\partial}{\partial T_{ve}} \ln Q_{e,i} + T_{ve} \frac{\partial^2}{\partial T_{ve}^2} \ln Q_{e,i} \right], \quad (4.13)$$

where $Q_{e,i} = \sum_j g_{i,j} \exp(-\Theta_{e,i,j}/T_{ve})$ is the canonical partition function for the electronic energy mode of species i . For the present study, in which we make use of the harmonic oscillator approximation, the vibrational specific heat for each species can be computed from

$$c_{v,v,i} = \frac{\mathcal{V}R^0}{\mathcal{M}_i} \left(\frac{\Theta_{v,i}}{T_{ve}} \right)^2 \frac{\exp(\Theta_{v,i}/T_{ve})}{(\exp(\Theta_{v,i}/T_{ve}) - 1)^2}. \quad (4.14)$$

With the exception of \mathcal{L}_1 for subsonic, positive convective velocities, all wave-amplitude variations can be directly computed at the outflow boundary with an upwind-biased scheme. However, \mathcal{L}_1 itself corresponds to an incoming wave at subsonic outflows, and thus can either be set to zero to yield a completely nonreflecting boundary or set to weakly impose a far-field pressure with $\mathcal{L}_1 = \kappa(P - P_\infty)$, as proposed in Poinot & Lele (1992). For the present study, in particular for the shock-turbulence simulation presented in Section 5, the latter approach is employed for computing \mathcal{L}_1 in order to weakly impose the outflow pressure and maintain the normal shock as nominally stationary.

5. Canonical shock-turbulence interaction

In order to verify the performance of the characteristic boundary conditions, direct numerical simulation of a canonical shock-turbulence interaction in thermal nonequilibrium is pursued with the present computational framework. As in Mahesh *et al.* (1997), performance is assessed based on a grid independence study to confirm that the numerical solution is insensitive to the post-shock extent of the computational domain. For the first shock-turbulence calculation, Case A, the domain extent is $(L_x/l, L_y/l, L_z/l) = (4\pi, 2\pi, 2\pi)$, where l is the reference length scale of 1 mm. An additional calculation,

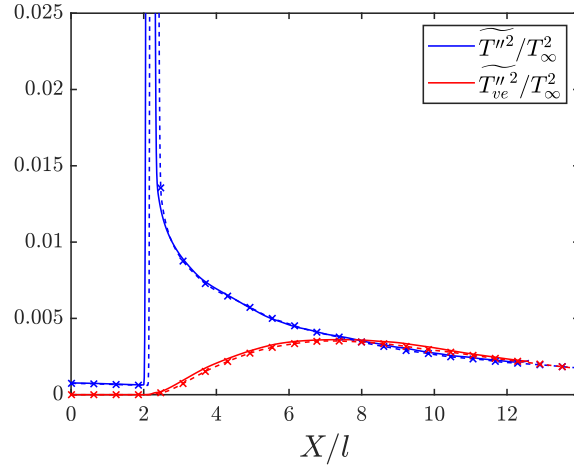


FIGURE 8. Favre variance of temperatures for shock-turbulence interaction in thermochemical nonequilibrium.

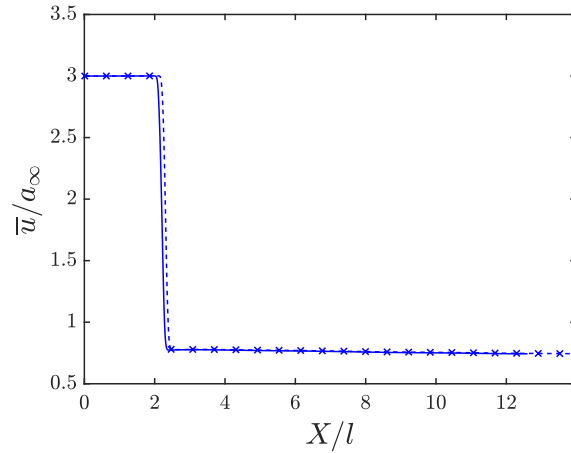


FIGURE 9. Favre-averaged streamwise velocity distribution for shock-turbulence interaction in thermochemical nonequilibrium.

Case B, is then performed with an extended post-shock region corresponding to a computational domain with side lengths $(L_x/l, L_y/l, L_z/l) = (6\pi, 2\pi, 2\pi)$. The grid spacing remains consistent across both simulations, with $(N_x, N_y, N_z) = (1024, 240, 240)$ for the smaller domain and $(N_x, N_y, N_z) = (1536, 240, 240)$ for the larger extent. In the present study, the Mach number is taken to be 3.0 for the shock-turbulence interaction, with the incoming turbulence characterized by a nominal Taylor-Reynolds number of 35 and a turbulent Mach number of 0.20. The freestream temperature is 700 K, with a static pressure of 8445.75 Pa, and, as such, the chemical composition is taken to be that of undissociated air: $Y_{N_2} = 0.79$, $Y_{O_2} = 0.21$. The turbulent inflow is generated by a concurrent homogeneous isotropic turbulence (HIT) calculation, with the inflow profiles transferred to the shock-turbulence computation at each time step. The constant-kinetic energy forcing of Bassenne *et al.* (2016) is applied within the HIT domain in order to maintain the turbulent inflow.

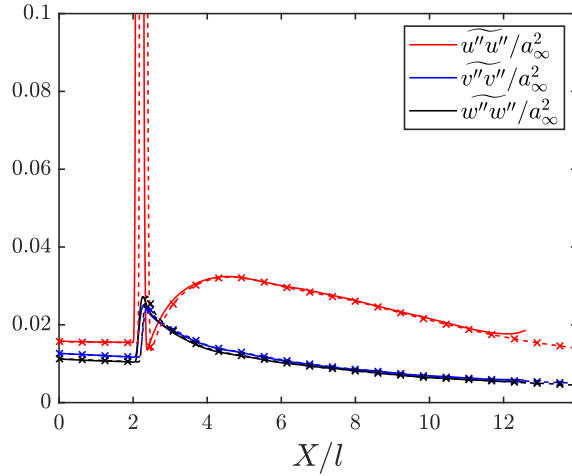


FIGURE 10. Reynolds stresses for shock-turbulence interaction in thermochemical nonequilibrium.

The direct numerical simulation results for the two-temperature shock-turbulence interaction are collectively presented in Figures 7–12, with the results from Cases A and B plotted with solid lines and dashed lines with symbols, respectively. The Favre averaging and fluctuation operators are denoted by $\overline{(\cdot)}$ and $(\cdot)''$, respectively, while $\overline{(\cdot)}$ and $(\cdot)'$ respectively represent the Reynolds averaging and fluctuation operators. Averaging is performed over approximately three eddy turnovers of the incoming turbulence and across the homogeneous direction of the shock-turbulence interaction. As depicted in Figure 7, significant vibrational-electronic nonequilibrium is induced by the presence of the normal shock, with vibrational relaxation proceeding through the subsonic outflow boundary. Comparison of the numerical solutions in Figures 7 and 8 reveals that both the Favre averages and variances of the temperatures remain largely independent of domain extent. Likewise, Figures 9 and 10 demonstrate the consistency of the Reynolds-averaged streamwise velocity and Reynolds stresses for both computational domains, confirming that the characteristic boundary conditions enable grid-independent numerical solutions. While Figure 11 clearly demonstrates that the presence of the artificial outflow boundary has no significant effect on the Reynolds-averaged pressure and density distributions, Figure 12 does suggest that numerical artifacts are introduced in the pressure variance in the immediate vicinity of the computational boundary. Further characterizing the sensitivity of the discrepancy in the pressure variance to domain size and evaluation of the κ parameter for computation of \mathcal{L}_1 are still required and will be the topic of future research.

6. Conclusions

A computational framework has been developed and implemented in the HTR solver in order to enable high-fidelity simulation of turbulent hypersonic flows in thermochemical nonequilibrium. The framework's novel elements include a high-order hybrid TENO/skew-symmetric scheme for inviscid flux evaluation, as well as characteristic boundary conditions for multicomponent reacting flows in thermal nonequilibrium. Performance of the inviscid flux reconstruction is verified by means of the reacting-air shock

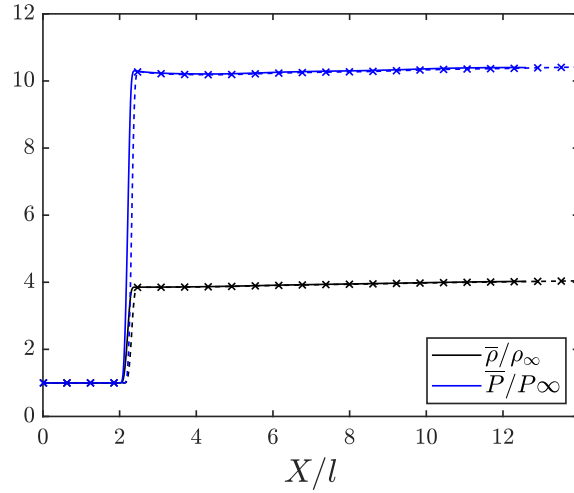


FIGURE 11. Reynolds-averaged density and pressure distributions for shock-turbulence interaction in thermochemical nonequilibrium.

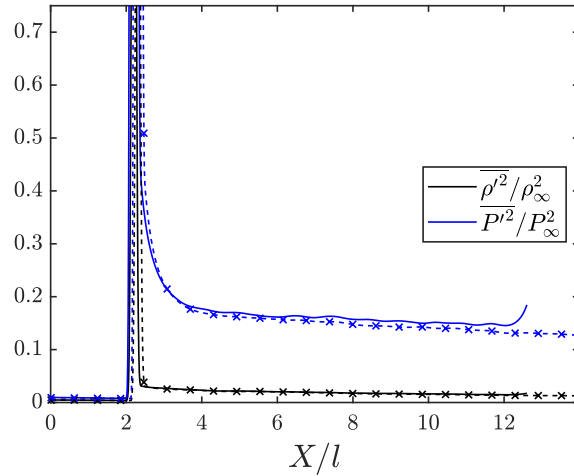


FIGURE 12. Variance of density and pressure for shock-turbulence interaction in thermochemical nonequilibrium.

tube of Grossman & Cinnella (1990), while the overall performance of the computational approach is confirmed via direct numerical simulation of a shock-turbulence interaction in thermochemical nonequilibrium. For this configuration, the two-temperature characteristic boundary conditions yielded consistent statistics of flow variables for varying computational domain extent. Future research activity will seek to further mitigate the pressure variance discrepancy at the subsonic outflow boundary and characterize its sensitivity to domain extent.

Acknowledgments

C.T.W. acknowledges support by the National Science Foundation Graduate Research Fellowship Program under Grant No. DGE-2146755. This investigation was funded by the Advanced Simulation and Computing (ASC) program of the US Department of Energy's National Nuclear Security Administration (NNSA) via the PSAAP-III Center at Stanford, Grant No. DE-NA0002373.

REFERENCES

- Bassenne, M., Urzay, J., Park, G. I. & Moin, P. 2016 Constant-energetics physical-space forcing methods for improved convergence to homogeneous-isotropic turbulence with application to particle-laden flows. *Phys. Fluids* **28**, 035114.
- CANDLER, G. V. 2019 Rate effects in hypersonic flows. *Annu. Rev. Fluid Mech.* **5**, 379–402.
- CANDLER, G. V. & MACCORMACK, R. W. 1991 Computation of weakly ionized hypersonic flows in thermochemical nonequilibrium. *J. Thermophys. Heat Tr.* **5**, 266–273.
- DI RENZO, M., FU, L. & URZAY, J. 2020 HTR solver: An open-source exascale-oriented task-based multi-GPU high-order code for hypersonic aerothermodynamics. *Comput. Phys. Comm.* **255**, 107262.
- DI RENZO, M. & URZAY, J. 2021 Direct numerical simulation of a hypersonic transitional boundary layer at suborbital enthalpies. *J. Fluid Mech.* **912**, A29.
- DI RENZO, M., WILLIAMS, C. T., URZAY, J. & PIROZZOLI, S. 2022 Stagnation enthalpy effects on turbulent Mach 5 compression corner flow. *Proceedings of the Summer Program*, Center for Turbulence Research, Stanford University.
- FU, L. & HU, X. Y. & ADAMS, N. A. 2016 A family of high-order targeted ENO schemes for compressible-fluid simulations. *J. Comput. Phys.* **305**, 333–359.
- GIMELSHEIN, S., WYSONG, I., FANGMAN, A., ANDRIENKO, D., KUNOVA, O., KUSTOVA, E., GARBACZ, C., FOSSATI, M. & HANQUIST, K. 2022 Kinetic and continuum modeling of high-temperature air relaxation. *J. Thermophys. Heat Tr.* **36**, 870–893.
- GNOFFO, P. A., GUPTA, R. N. & SHINN, J. L. 1989 Conservation equations and physical models for hypersonic air flows in thermal and chemical nonequilibrium. *Tech. Pap.* 2867, NASA.
- GROSSMAN, B. & CINNELLA, P. 1990 Flux-split algorithms for flows with nonequilibrium chemistry and vibrational relaxation. *J. Comp. Phys.* **88**, 131–168.
- HUETE, C., CUADRA, A., VERA, M. & URZAY, J. 2021 Thermochemical effects on hypersonic shock waves interacting with weak turbulence. *Phys. Fluids* **33**, 086111.
- LARSSON, J. & LELE, S.K. 2016 Direct numerical simulation of canonical shock/turbulence interaction. *Phys. Fluids* **21**, 126101.
- JIANG, G. S. & SHU, W. S. 1996 Efficient implementation of weighted ENO schemes. *J. Comp. Phys.* **126**, 202–228.
- LEE, S., LELE, S.K. & MOIN, P. 1993 Direct numerical simulation of isotropic turbulence interacting with a weak shock wave. *J. Fluid Mech.* **251**, 533–562.
- LEE, S., LELE, S.K. & MOIN, P. 1997 Interaction of isotropic turbulence with shock waves: Effect of shock strength. *J. Fluid Mech.* **340**, 225–247.
- LUSHER, D. J., & SANDHAM, N. D. 2021 Assessment of low-dissipative shock-capturing schemes for the compressible Taylor–Green vortex. *AIAA J.* **59**, 533–545.

- MAHESH, K., LELE, S.K. & MOIN, P. 1997 The influence of entropy fluctuations on the interaction of turbulence with a shock wave. *J. Fluid Mech.* **334**, 353–379.
- MAIER, W. T., NEEDELS, J. T., GARBACZ, C., MORGADO, F., ALONSO, J. J. & FOSSATI, M. 2021 SU2-NEMO: An open-source framework for high-Mach nonequilibrium multi-species flows. *Aerospace* **8** 193–222.
- OKONG’O, N. & BELLAN, J. 2002 Consistent boundary conditions for multicomponent real gas mixtures based on characteristic waves. *J. Comput. Phys.* **176**, 330–344.
- PARK, C. 1990 *Nonequilibrium Hypersonic Aerothermodynamics*. Wiley.
- PASSIATORE, D., SCIACOVELLI, L., CINNELLA, P., & PASCAZIO, G. 2022 Thermochemical non-equilibrium effects in turbulent hypersonic boundary layers. *J. Fluid Mech.* **941**, A21.
- PIROZZOLI, S. 2010 Generalized conservative approximations of split convective derivative operators. *J. Comput. Phys.* **229**, 7180–7190.
- POINSOT, T. J. & LELE, S. K. 1992 Boundary conditions for direct simulations of compressible viscous flows. *J. Comput. Phys.* **101**, 104–129.
- WILLIAMS, C. T., DI RENZO, M. & URZAY, J. 2021 Two-temperature extension of the HTR solver for hypersonic turbulent flows in thermochemical nonequilibrium. *Annual Research Briefs*, Center for Turbulence Research, Stanford University, pp. 95–107.